Journal of Biomechanics 53 (2017) 15–21

Contents lists available at ScienceDirect

Journal of Biomechanics

journal homepage: www.elsevier.com/locate/jbiomech
www.JBiomech.com

Postoperative analysis of the mechanical interaction between stent and host tissue in patients after transcatheter aortic valve implantation

Raoul Hopf[a,*,1], Simon H. Sündermann[c,1], Silvia Born[d], Carlos E. Ruiz[f], Nicolas M. Van Mieghem[g], Peter P. de Jaegere[g], Francesco Maisano[e], Volkmar Falk[c], Edoardo Mazza[a,b]

[a] Institute of Mechanical Systems, Department of Mechanical Engineering, Swiss Federal Institute of Technology (ETH), Switzerland
[b] Swiss Federal Laboratories for Materials Testing and Research, EMPA Dübendorf, Switzerland
[c] Department of Cardiothoracic and Vascular Surgery, Deutsches Herzzentrum Berlin, Germany
[d] Hybrid Laboratory for Cardiovascular Technologies, University of Zurich, Switzerland
[e] Division of Cardiovascular Surgery, University Hospital Zurich, Switzerland
[f] Structural and Congenital Heart Center, Hackensack University Medical Center and the Joseph M. Sanzari Children's Hospital, Hackensack, NJ, USA
[g] Department of Cardiology, Thoraxcenter, Erasmus Medical Center, Rotterdam, The Netherlands

ARTICLE INFO

Article history:
Accepted 19 December 2016

Keywords:
TAVI
Aortic stent
Corevalve
Simulation
Contact forces
Postoperative analysis

ABSTRACT

The analysis is based on a finite element procedure to extract the contact forces between an implanted Nitinol stent and the surrounding host tissue using postoperative CT images. The methodology was applied for patients ($N=46$) which have undergone a TAVI procedure with the Medtronic CoreValve Revalving System (MCRS) to obtain corresponding deformation and force maps. The postoperative CT data were recorded for each patient in both systolic and diastolic phase of the heart cycle. Scalar parameters were defined, which map deformed geometry and contact force field to mechanically relevant quantities: radial dilatation, radial shape distortion, non-convex points, mean force, a force deviation measure and a pressure equivalent. The latter demonstrates that in the area of the aortic root, the added circumferential loading is of the same order as the baseline average blood pressure, thus leading to a doubling of the local mechanical load. Generally the force distribution along the stent is non-homogeneous. A comparison of systolic and diastolic data revealed slightly higher contact forces during the diastole, indicating that the stent has to carry more load in this phase. The geometrical and mechanical parameters were compared for two types of clinical complication: para-valvular leakage (PVL) and permanent pacemaker requirement (PPM). It was found that an increase in mean force can be associated with both complications; significantly for PVL and as a trend for PPM.

1. Introduction

Biocompatibility is a fundamental requirement for the successful application of any medical implant. In recent years the concept of "mechanical biocompatibility" has been introduced to discuss the relevance of the mechanical interaction between host tissue and implant. For example, medical mesh implants used in hernia or pelvic floor prolapse repair can cause significant complications due to unfavorable mechanical behavior of the implanted structure (Maurer et al., 2014). A general discussion and overview on mechanical biocompatibility of highly deformable implants was given in Mazza and Ehret (2015). Investigations that lead to a better understanding of the underlying mechanics which lead to pathological outcomes may contribute to improved implant design and new procedures.

Particularly critical questions of mechanical biocompatibility arise in the application of transcatheter aortic valve implantation (TAVI): a possible complication associated with malfunctioning of the device is aortic regurgitation (AR) which can lead to weakened pressure gradients during the cardiac cycle and cause general heart insufficiency. A more indirect complication is the permanent pacemaker requirement (PPM) which is caused by total or partial blockage of the atrio-ventricular (AV) node. In the early stages of TAVI development, these complications were already described by Cribier et al. (2002). The application in the present work focuses on the characterization of the mechanical interaction between a Nitinol TAVI stent and its surrounding aortic valve complex in patients after TAVI using postoperative patient data.

* Corresponding author.
E-mail address: hopf@imes.mavt.ethz.ch (R. Hopf).
[1] These two authors contributed equally.

http://dx.doi.org/10.1016/j.jbiomech.2016.12.038
0021-9290/

A significant number of clinical studies on TAVI and associated complications have been performed in recent years. A meta-analysis by Jilaihawi et al. (2012a) compares two different valve types for TAVI (Edwards SAPIEN and Medtronic CoreValve) with the standard surgical aortic valve replacement (SAVR) and concluded that for most complications no significant differences are observable. Among other criteria, they considered the risk of 30 day stroke and dialysis inception. However, they found a significant difference in permanent pacemaker requirement (PPM) between both valve types (24.5% for the CoreValve vs 5.9% for the SAPIEN with $P < 0.0001$) and they report a rate of 11% for aortic regurgitation (AR). Several papers focused on anatomical, physiological and clinical factors associated with AR (Abdel-Wahab, 2011; Jilaihawi et al., 2012a,b; Athappan et al., 2013) and PPM (Jilaihawi et al., 2009; Khawaja et al., 2011; Erkapic et al., 2010; De Carlo et al., 2012; Rubin et al., 2011; Goldenberg et al., 2013). It has to be emphasized that the complication rates have significantly decreased over the past years. In the case of para-valvular leakage (as a subgroup of AR), there is always a mismatch between the implanted valve and the native geometry of the host tissue. Some of the current research states that in particular PVL is a result of either valve under sizing or high calcium score and that implantation depth is a further significant indicator attributed to this complication (Abdel-Wahab, 2011; Athappan et al., 2013; Takagi et al., 2011; Detaint et al., 2009; Clavel et al., 2009; Sherif et al., 2010). The causes of AV node blockage and subsequently to PPM are more complex (Moreno et al., 2009). Generally, it is speculated that stresses due to mechanical loading, induced by the deployment procedure and by the stent–tissue interaction after implantation, lead to either direct tissue damage and thus to a deterioration of electrical conductivity in the corresponding cells, or cause microscopic hematomas which again lead to damaging of cells locally (Goldenberg et al., 2013; Rubin et al., 2011; Moreno et al., 2009).

The present work provides for the first time quantitative information on the mechanical interaction between stent and aortic root based on a finite element analysis of postoperative CT images of the first generation CoreValve stent by Medtronic. Previous studies which used finite element computations incorporating patient specific geometries (such as for example the work by Auricchio et al., 2014; Morganti et al., 2016) have focused on developing complex contact-based simulations, where only a very small number of patients could be analyzed. Other studies also included computational fluid dynamics in order to predict AR (de Jaegere et al., 2016) or used FE models to study the valve morphology and calcium displacement (Schultz et al., 2016). In the present work, an effective numerical modeling technique is applied which allowed faster postoperative outcome analysis of TAVI patients to quantitatively characterize the mechanical interaction of stent and host tissue. The methods proposed by Gessat et al. (2014) were implemented to obtain a procedure for the automatic extraction of contact forces between stent and host tissue for patients after TAVI. This procedure was applied to a larger patient data set ($N=46$) to obtain the corresponding force fields in *both* the *diastolic* and *systolic* phase of the heart cycle for each patient. The magnitude of these force vectors as well as their fluctuation during the cardiac cycle is indicative of the mismatch with respect to physiological mechanical loading conditions of the aortic root, as well as of the fatigue loading of the device. This information is relevant for device optimization, in view of future extension of the TAVI procedure to a wider patients age range.

2. Material and methods

2.1. Patient data

The patient data sets were provided by three different heart centers: Lenox Hill Heart and Vascular Institute (New York, USA), Thorax Center of the Erasmus Universiteit (Rotterdam, Netherlands) and the Division of Cardiovascular Surgery at University Hospital of Zurich (Zurich, Switzerland). The resolution of the image acquisition systems used in the three heart centers are similar, so that a qualitative equivalence could be assumed for all image data-set included in the present analysis. Table 1 summarizes the data sets which are considered in this postoperative analysis. For this retrospective study routinely acquired postoperative CT scans were used, and all data were anonymized. The complications in discussion here are para-valvular leakage (PVL) and the indication for a new pacemaker after implantation (PPM). In the postoperative ultrasound examination the severity of leakage was determined and assigned a number from 1 to 3, where 1 corresponds to minimal leakage, 2 to moderate leakage and 3 to severe leakage. Four of the patients displayed both pathologies. Only patients with moderate to severe aortic regurgitation are considered as PVL cases for the present analysis. Our data set shows a similar rate of PPM as the meta-analysis by Jilaihawi et al. (2012a). However, they reported an overall rate for both stents together of around 11% for issues related to AR, whereas our data set displays 46% incidence for PVL alone, which does not include other AR occurrences, such as trans-valvular leakage. Athappan et al. (2013) reported an overall rate of AR of around 16% for the CoreValve stent in particular, which is still significantly lower than our data suggests. This could be attributed to differences in the threshold definitions used for the classification between mild, moderate and severe. Postoperative CT scans of systolic and diastolic phase of each patient were used to extract the deformed geometry of the stent. A beam element based finite element simulation is performed assigning the measured deformed configuration of the stent as kinematic boundary condition (i.e. a displacement controlled simulation, in which nodal displacements are applied with an additional compliance) and determining the external forces required to achieve this deformed state, as described in Gessat et al. (2014). In this case the Timoshenko type element B31 of the ABAQUS standard library has been selected, as it performs very well under finite angle rotations and was previously shown to provide reliable results in stenting applications (Hall and Kasper, 2006). Based on the principle of action equals reaction, these forces represent the mechanical loads acting on the aortic root. As explained in Gessat et al. (2014), determination of forces between stent and aortic wall does not require knowledge of mechanical properties of the aortic tissue.

2.2. CoreValve geometry and analysis

The stent consists of 30 strings and has 165 intersection nodes where (see Fig. 1), according to the FE model, contact forces are calculated. The nodes can be organized as a layer structure that consists of 11 *layers* with 15 nodes each. In the deformed configuration nodes in a layer lay only approximately in a plane. An indexed position vector notation $\mathbf{p}_{ij}$ is adopted to address all points individually, where the index $i \in \{0, \ldots, 10\}$ refers to the layer and the index $j = \{0, \ldots 14\}$ denotes the point within the layer. Layer 0 is set at the proximal end of the structure. Similarly, corresponding forces are denoted with $\mathbf{F}_{ij}$. A *section* denotes the set of points with a fixed index j within all layers (points do not lie on a straight line), thus the stent can be divided into 15 sections. The leaflet area (LA) is defined as layers 0–6. The simulation output for each patient yields a contact force field and a displacement vector field. In this context "contact force" always refers to the normal components of the contact force. These components are computed by estimating the surface normal of the host tissue from the deformed geometry of the stent. For the subsequent outcome analysis, several scalar parameters which represent geometric or force-based quantities in each layer of the stent are introduced. These parameters are then visualized, discussed in the context of mechanical interaction, and with respect to the corresponding clinical outcomes.

2.3. Geometric parameters

2.3.1. Layer distortion

Generally, the layer distortion LD_i of any layer i is computed by defining it as a deviation measure from a perfect circle. First, the canonical geometric center $\mathbf{s}_i$ of the points $\mathbf{p}_{ij}$ in the layer is determined. Then, the average distance R_m from the center $\mathbf{s}_i$ to all points $\mathbf{p}_{ij}$ is obtained. Lastly, LD_i for the i-th layer is defined as a deviation measure of the distances from $\mathbf{s}_i$ to the points $\mathbf{p}_{ij}$ in the layer

$$\mathbf{s}_i = \sum_{j=0}^{14} \frac{1}{15} \mathbf{p}_{ij} \tag{1}$$

$$R_m = \sum_{j=0}^{14} \frac{1}{15} \| \mathbf{s}_i - \mathbf{p}_{ij} \| \tag{2}$$

Thus, the layer distortion (see Fig. 2) is defined by

$$LD_i = \sqrt{\sum_{j=0}^{14} \left(\frac{\| \mathbf{s}_i - \mathbf{p}_{ij} \|}{R_m} - 1 \right)^2} \tag{3}$$

2.3.2. Non-convex points

If all points $\mathbf{p}_{ij}$ in a layer are projected into their regression plane, a convex hull to the point set can be identified in the regression plane. This is done for each layer i. Fig. 3 illustrates the concept of non-convex points in the plane

$$NCP_i = \#\text{of non} - \text{convex points in layer } i. \tag{4}$$

Generally, it is expected that all points belong to the convex hull. However, it is possible that large chunks of a calcium deposit could lead to further local radial compression of a (or multiple adjacent) point(s) (convex points are only identified up to a tolerance measure, which is compared to the distance of the point to the convex hull). Furthermore, if a structural instability exists in the stent, a "snapping" motion could lead to non-convex points only appearing at certain time points of the cardiac cycle. The convex hull is computed using the QHull library (QHull.org, 2016), which has pre-compiled Python wrappers available.

2.3.3. Layer area dilatation

Here a local measure of area change is introduced, which corresponds to a single layer. The area of a layer is computed for both reference and deformed state for layers projected into their regression plane. The projection of a point $\mathbf{p}_{ij}$ is addressed in the corresponding regression plane (in a local coordinate system) by $\mathbf{x}_{ij} = \left(x_{ij}^1, x_{ij}^2, 0\right)^T$. Capital letters refer to the undeformed reference configuration.

$$A_i = \frac{1}{2} \sum_{j=0}^{13} \| \mathbf{X}_{ij} \times \mathbf{X}_{ij+1} \| \tag{5}$$

$$a_i = \frac{1}{2} \sum_{j=0}^{13} \| \mathbf{x}_{ij} \times \mathbf{x}_{ij+1} \| \tag{6}$$

The area dilatation for each layer is then given by

$$AD_i = \frac{a_i}{A_i} \tag{7}$$

For the implanted stent values of AD_i are expected to be < 1, indicating an area contraction.

Table 1
An overview of the data sets used for the post-operative outcome analysis of TAVI patients. This data set only includes patients where both systolic and diastolic scans were available and could be segmented properly. The bottom row shows the frequencies of the three different diameter sizes that were present in our dataset.

Patients	**PVL**	**PPM**	**PVL+PPM**
46	21 (46%)	10 (22%)	4 (9%)
	CV 26	**CV 29**	**CV 31**
	16 (35%)	24 (52%)	6 (13%)

2.4. Force based parameters

2.4.1. Mean force per layer

The first force based measure is simply the mean force of all contact forces each layer. High average forces correspond to high average deformation or very high local peaks.

$$MF_i = \frac{1}{15} \sum_{j=0}^{14} \| \mathbf{F}_{ij} \| \tag{8}$$

2.4.2. Deviation of force measure per layer

The standard deviation measure for the force values for each layer i is introduced as

$$DF_i = \sqrt{\frac{1}{15} \sum_{j=0}^{14} \left(MF_i - \| \mathbf{F}_{ij} \| \right)^2} \tag{9}$$

2.5. Pressure equivalent per layer

In order to obtain a parameter which joins forces and geometry together with a dependence of the actual stent size and encodes a loading measure that can be compared to a typical medical parameter, a pressure equivalent was defined and evaluated in mmHg. This pressure equivalent PEQ_i is defined by dividing the

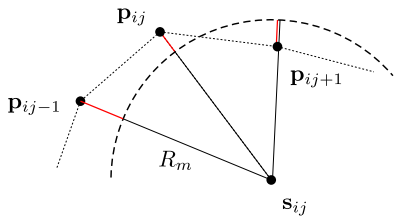

Fig. 2. The distortion measures the relative deviation from the average circular radius R_m at each point $\mathbf{p}_{ij}$ in a layer.

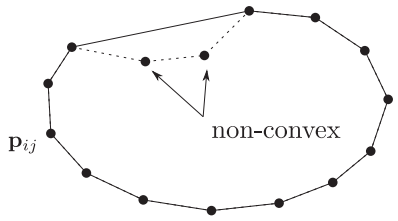

Fig. 3. Non-convex points are all points that do not belong to the convex hull of the cross section of the stent.

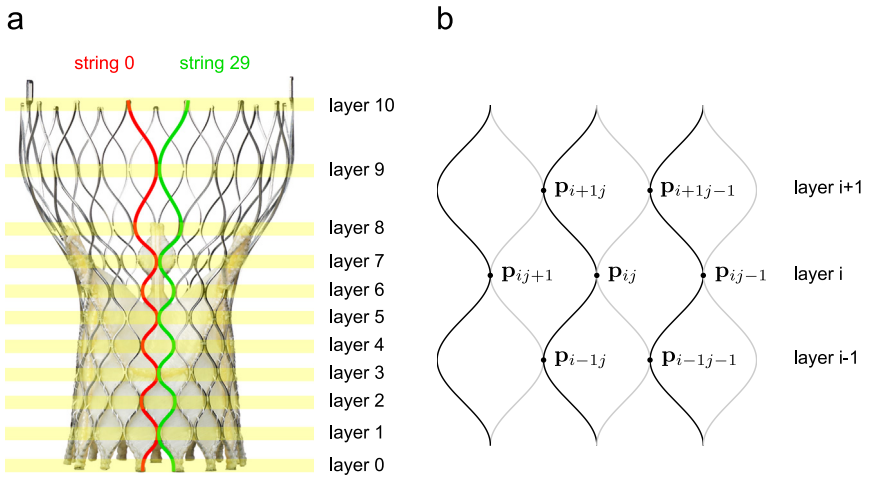

Fig. 1. Basic geometric parameter definitions on the CoreValve: The stent can be divided into 11 layers (a). Each layer holds 15 intersection points $\mathbf{p}_{ij}$. There are 30 physical strings, which impose a node connectivity pattern for the intersections (b). Layers 0–6 constitute the leaflet area.

contact force f_i of the layer by the corresponding area a_i^{wall} in the deformed configuration

$$f_i = \sum_{j=0}^{14} \| \mathbf{F}_{ij} \| \tag{10}$$

$$\Delta h_i = \| \mathbf{s}_{i+1} - \mathbf{s}_i \| \tag{11}$$

$$u_i = \sum_{j=0}^{14} \| \mathbf{p}_{ij} - \mathbf{p}_{ij+1} \| \tag{12}$$

$$a_i^{\text{wall}} = \frac{1}{2}(u_i \Delta h_i + u_{i+1} \Delta h_i) \tag{13}$$

Eq. (13) is an area estimator that approximates the outer hull of the stent for each layer. This is achieved by computing the distances between layers (heights) and all the circumferences of the layers and multiplying each height with the lower and upper layer circumference yielding upper and lower bounds for the outer hull, which then are averaged. Finally, the equivalent pressure per layer is given by

$$PEQ_i = \frac{f_i}{a_i^{\text{wall}}} \tag{14}$$

3. Results and discussion

Fig. 4 shows the area dilatation and the mean force for the systolic and diastolic phase of a representative case in axial view. Rather than showing averaged data, a representative case was chosen in order to show deformation and force data that physically correspond to each other. Higher forces (in particular in the leaflet area where the stent is radially most stiff) and correspondingly increased area compression are visible for the systolic phase. The deformation induced by the blood pressure difference is modest which can be associated with a relatively stiff behavior of the aortic root. The typical inhomogeneity of forces and deformations along the stent is demonstrated in this figure. Interestingly, the distribution of contact forces could not be predicted based solely on the pattern of area dilatation. In particular, the contact force level decreases along the leaflet area (where the area dilatation is relatively constant) even though the radial stiffness increases in this area. This is a result of the kinematic coupling within the structure, mainly induced by the second region of high mechanical interaction, which is at the distal extremity of the stent (layer 9).

The mean forces show a decrease on both ends (layers 0 and 10). This can be attributed to a lower radial stiffness, since these intersection points are only connected one side. In addition, due to the particular structure of the CoreValve, the points in layer 10 are expected to show a minimum of radial force: here, the adjacent mesh loops are very large, which leads to elevated radial compliance; since layer 9 has the largest diameter in the undeformed state, the points in layer 10 are expected to be just passively radially compressed, induced by the global stent motion and exhibit little to no contact with the aortic wall.

3.1. Mechanical loading of the aortic wall

The deformation of the stent is associated with a concentrated stress distribution along all strut surfaces which are in contact with tissue. This is a localized radially outward force on the tissue which is added to the blood pressure. Both, radial forces from the stent and blood pressure contribute to circumferential stretching of the aortic root. This also motivated the definition of the equivalent pressure measure. A qualitative depiction of the added loading due to stent forces is given in Fig. 5. The deformation of the stent would be at a theoretical maximum in the complete absence of blood pressure and would reach zero above some pressure threshold (for which the aortic root would be theoretically deformed to a diameter larger than the one of the undeformed stent). The total load on the arterial wall is the sum of the loading from stent and blood pressure and is at unphysiologically high levels at all times in the area of the implant.

The equivalent pressure measure PEQ_i allows to quantify this additional load, see Fig. 6. Considering average values shows that the equivalent pressure is in the order of magnitude of average blood pressure, meaning that in the region of the implanted stent the load on the tissue is roughly doubled. Note however that due to the mesh-like structure of the stent the physical contact surfaces are small and thus local pressure peaks will occur which are significantly larger than the average equivalent pressure. On the other hand, the resulting circumferential loading of the tissue can be reliably characterized with the equivalent pressure value.

3.2. Para-valvular leaks

Para-valvular leakage is only visible during the diastole, so that the analysis focused on diastolic data. Fig. 7 depicts area dilatation, layer distortion and mean force for each of the 11 layers. The data set was split into two groups: patients without para-valvular leaks and patients with leaks. Since PVL is commonly associated with valve under sizing, the intuitive expectation was to obtain lower averages of contact force together with lower values of radial compression in pathological situations. However, observations of our data set display the opposite: PVL patients display a significantly ($p=0.009$ for systolic and $p=0.079$ for diastolic) higher mean force in layers 0–7 and accordingly higher layer area compression. This behavior was also previously observed in Morganti et al. (2014). Larger compressive forces are indicative of a stiff aortic tissue. It seems plausible that lower compliance of the aortic

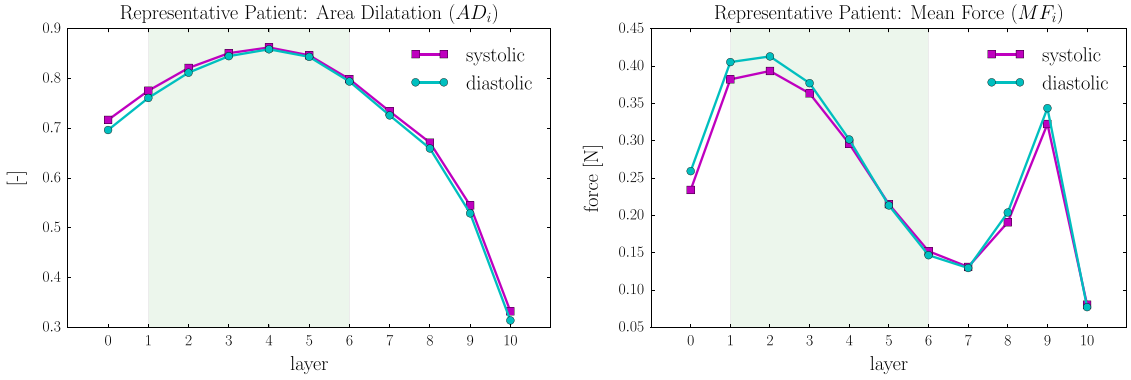

Fig. 4. Area dilatation and mean force for a representative patient case. A small increase of compression during diastole and slightly elevated mean forces in the leaflet area (indicated with the light green rectangular area) can be observed. (For interpretation of the references to color in this figure caption, the reader is referred to the web version of this paper.)

root leads to an impairment of the local sealing ability of the stent–wall interface. Furthermore, the distortion of layers is larger in case of PVL (but the difference is not statistically significant). This might be associated with increased local forces: when considering larger volumes of native leaflets calcifications, enhanced local compression in the leaflet area can occur leading to a loss of seal. The representation in Fig. 7 highlights the large differences in force magnitude at different circumferential locations, with large forces occurring in a specific contact region while in other intersection points the compressive loads are very low. It is also interesting to note that a priori estimation of where the peaks of the contact forces will be localized based solely on the layer deformation is not possible.

In our data set, only three patients displayed non-convex points (see Fig. 8), all of which had PVL. A possible hypothesis is that non-convexities might be associated with local calcifications. This should be verified with dedicated imaging of the corresponding region.

3.3. Permanent pacemaker requirement

In the case of permanent pacemaker requirement, higher contact forces were expected, since this leads to an increase in stresses in the aortic root tissue, which might be responsible for damage in conductive cells and thus for AV node blockage. Looking at Fig. 9, it can be seen that in the case of PPM, normal contact forces and radial compression are in average increased over non-PPM patients. For the mean force of layers 0–6 a corresponding trend can be found and, to a lesser extent, for the area dilatation. In Fig. 9 on the right-hand side the standard deviation of the force is shown. Patients with permanent pacemaker requirement show significantly ($p=0.041$ for systolic and $p=0.047$ for diastolic) lower deviation measures for contact force in the leaflet area. This might indicate that in average the rise in contact forces also corresponds to a more homogeneous force field in case of PPM.

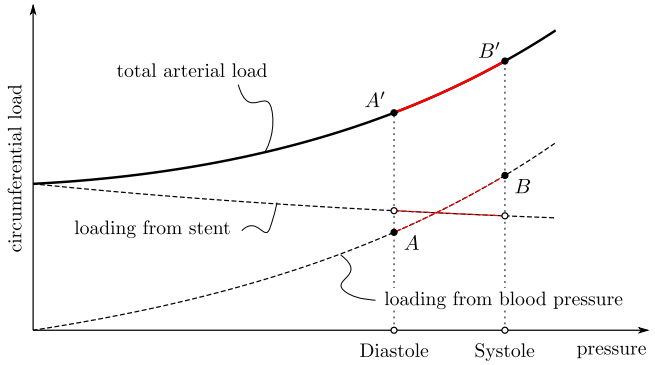

Fig. 5. Qualitative depiction of the circumferential loading of the arterial wall as a function of the blood pressure: the loading component of the stent is at a maximum when there is no loading by the blood pressure. Without implant, the loading would be cycling between points A and B. The addition of the stent leads to an elevated cycle between points A' and B'.

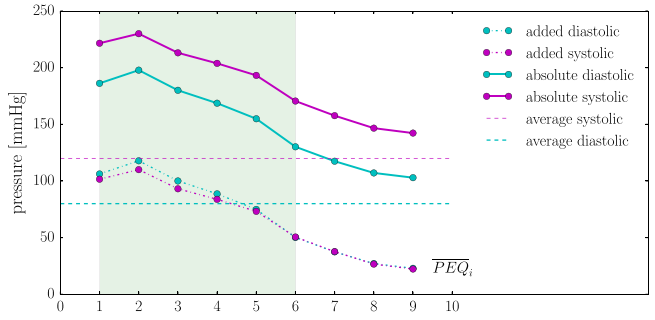

Fig. 6. Layer-wise plot of the equivalent pressure: average values for all patients. The dashed straight lines indicate the average human blood pressure in both phases of the heart cycle. The dotted lines correspond to the added pressure in each layer. Both full lines depict the absolute values of pressure-loading in the area, which is the sum of the blood pressure and stent loading. The shaded rectangle indicates the leaflet area.

4. Conclusions

A database of 46 patients was analyzed using a FE based procedure, where systolic and diastolic images were available for each individual patient. The outcome analysis consisted of the definition of geometric and force based features, which aimed at providing parameters for the characterization of the mechanical interaction between stent and aortic root. In addition, parameters were used to evaluate pathological cases. Algorithms were defined to automatically extract these features from the results of the numerical calculations. The findings indicate that in average large radial forces are present in the leaflet region. Their magnitude corresponds to a structural overloading of the aortic wall, corresponding to about two times the physiological level associated with blood pressure. The distribution of forces along the stent indicates large differences with regions of high and regions of low contact forces. It is expected that a more homogeneous distribution of radial forces would ensure the same positional stability without excessive local tissue loading. Difference between systolic and diastolic was quantified for stent deformation and forces. This information could be used to quantify the expected fatigue loading of the stent structure. The results of the outcome analysis

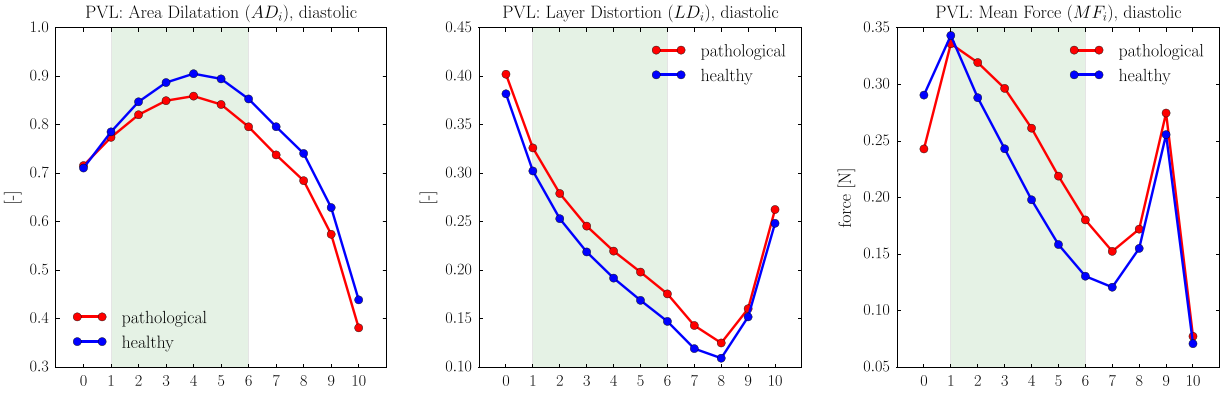

Fig. 7. Layer-wise defined parameters in axial view. Patients are split into PVL and healthy sets and parameters are shown in diastolic configuration. The shaded rectangle indicates the leaflet area.

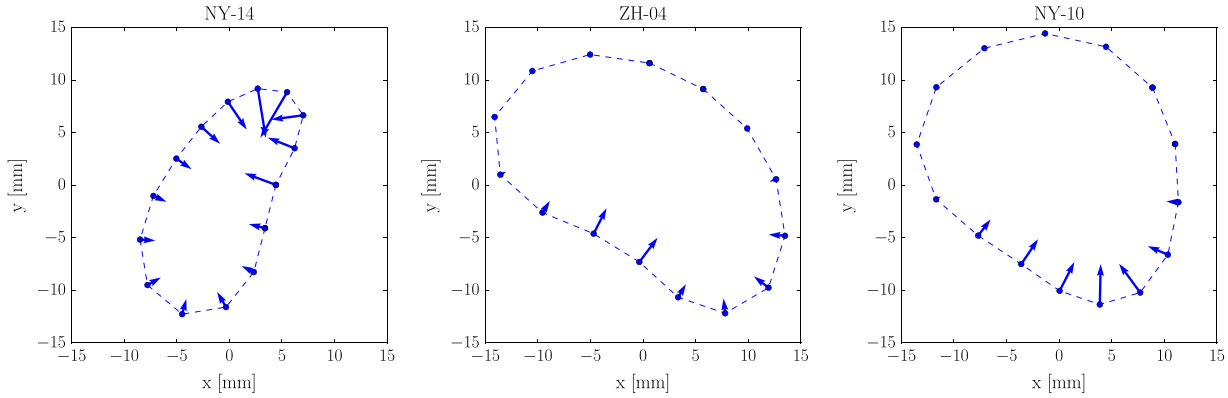

Fig. 8. Three patients that display non-convex in proximal layers (diastolic, layer L_1 displayed in all cases). The vectors depict normal components of the contact forces. All three patients that display non-convex points had PVL.

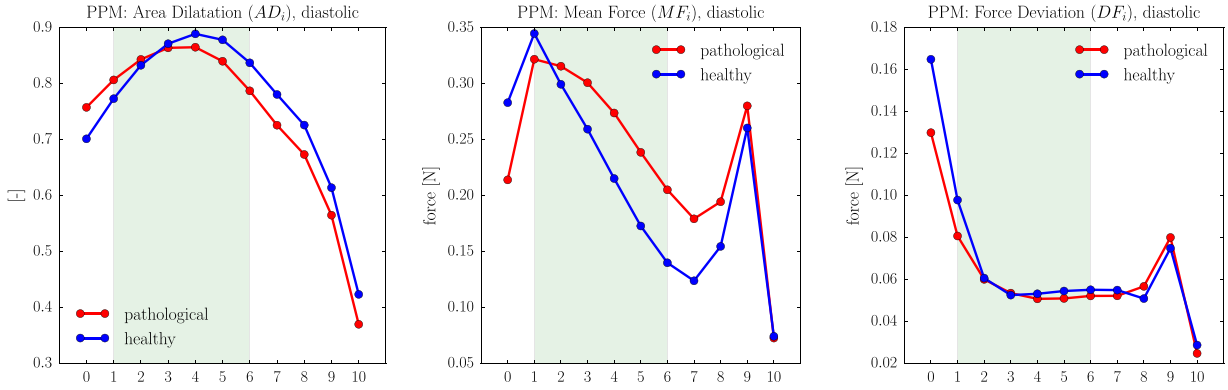

Fig. 9. Layer-wise defined parameters in axial view. Patients are split into PPM and healthy sets and parameters are shown in diastolic configuration. The shaded rectangle indicates the leaflet area.

indicated that the mechanisms associated with complications are more complex than initially expected. In the case of PVL it was observed that instead of decreased, elevated reaction forces are present. This effect might be due to the fact that a higher aortic wall stiffness leads to reduced contact compliance and thus impaired sealing ability at the stent–tissue interface. AR is also connected with more distorted stent shapes. In the case of PPM we found higher forces and more homogeneous force fields. This result supports the hypothesis that stronger loading of the aortic tissue might contribute to AV node blockage.

As mentioned in the Introduction, there are further important factors which were not considered in this analysis. Most important from the mechanical viewpoint is the influence of the constitutive behavior of the aortic tissue. In fact, large contact forces are only one side of the problem and as for any structural assessment problem, the criticality of a loading condition depends also on the corresponding state of deformation of the material and the corresponding limits. Furthermore, mechanical parameters should be associated with previously identified such as anatomical and physiological characteristics as well as stent placement and sizing (Abdel-Wahab, 2011; Athappan et al., 2013; Clavel et al., 2009; Detaint et al., 2009; Sherif et al., 2010; Takagi et al., 2011).

While the rate of complications in TAVI is significantly decreased, the envisaged extension of the age range of application of this minimally invasive procedure will be linked with new challenges. In particular, questions arise concerning the long-term response of aortic tissue and stent when subjected to the increased steady load and its fluctuations. In a next analysis step, correlations between mechanical parameters and clinical factors (such as patient age and gender, device size and the degree of PVL) will be analyzed. The data and the methodology presented in this paper provide a basis for the optimization of stent design and medical procedures. An important limitation of the proposed methodology is that it is not predictive, since it requires the deployed stent shape as in input. Future investigations might provide a prediction of stent contact force based on patient specific information on pre-operative aortic geometry and deformability (e.g. through elastography). Such an extended approach might be used preoperatively to guide the selection of stent type and size.

Conflict of interest statement

None declared.

Acknowledgments

The project was supported by the Swiss National Science Foundation (SNSF, Project no. CR32I3 135044), the Swiss Heart Foundation, the Stiftung PROPTER HOMINES – Vaduz/Fürstentum Liechtenstein, the Schwyzer-Winiker Stiftung and the ETH Zurich Foundation.

References

Abdel-Wahab, M., Zahn, R., Horack, M., Gerckens, U., Schuler, G., Sievert, H., Eggebrecht, H., Senges, J., Richardt, G., 2011. Aortic regurgitation after transcatheter aortic valve implantation: incidence and early outcome. Results from the German transcatheter aortic valve interventions registry. Heart 97 (11), 899–906.

Athappan, G., Patvardhan, E., Tuzcu, E.M., Svensson, L.G., Lemos, P.A., Fraccaro, C., Tarantini, G., Sinning, J.-M., Nickenig, G., Capodanno, D.E.A., 2013. Incidence, predictors, and outcomes of aortic regurgitation after transcatheter aortic valve replacement. J. Am. Coll. Cardiol. 61 (15), 1585–1595.

Auricchio, F., Conti, M., Morganti, S., Reali, A., 2014. Simulation of transcatheter aortic valve implantation: a patient-specific finite element approach. Comput. Methods Biomech. Biomed. Eng. 17 (12), 1347–1357.

Clavel, M.-A., Webb, J.G., Pibarot, P., Altwegg, L., Dumont, E., Thompson, C., De Larochellière, R., Doyle, D., Masson, J.-B., Bergeron, S.E.A., 2009. Comparison of the hemodynamic performance of percutaneous and surgical bioprostheses for the treatment of severe aortic stenosis. J. Am. Coll. Cardiol. 53 (20), 1883–1891.

Cribier, A., Eltchaninoff, H., Bash, A., Borenstein, N., Tron, C., Bauer, F., Derumeaux, G., Anselme, F., Laborde, F., Leon, M.B., 2002. percutaneous transcatheter implantation of an aortic valve prosthesis for calcific aortic stenosis first human case description. Circulation 106 (24), 3006–3008.

De Carlo, M., Giannini, C., Bedogni, F., Klugmann, S., Brambilla, N., De Marco, F., Zucchelli, G., Testa, L., Oreglia, J., Petronio, A.S., 2012. Safety of a conservative strategy of permanent pacemaker implantation after transcatheter aortic corevalve implantation. Am. Heart J. 163 (3), 492–499.

de Jaegere, P., De Santis, G., Rodriguez-Olivares, R., Bosmans, J., Bruining, N., Dezutter, T., Rahhab, Z., El Faquir, N., Collas, V., Bosmans, B.E.A., 2016. Patient-specific computer modeling to predict aortic regurgitation after transcatheter aortic valve replacement. JACC: Cardiovasc. Interv. 9 (5), 508–512.

Detaint, D., Lepage, L., Himbert, D., Brochet, E., Messika-Zeitoun, D., Iung, B., Vahanian, A., 2009. Determinants of significant paravalvular regurgitation after transcatheter aortic valve implantation. JACC: Cardiovasc. Interv. 2 (9), 821–827.

Erkapic, D., Kim, W.K., Weber, M., Mollmann, H., Berkowitsch, A., Zaltsberg, S., Pajitnev, D.J., Rixe, J., Neumann, T., Kuniss, M.E.A., 2010. Electrocardiographic and further predictors for permanent pacemaker requirement after transcatheter aortic valve implantation. Europace 12 (8), 1188–1190.

Gessat, M., Hopf, R., Pollok, T., Russ, C., Frauenfelder, T., Sundermann, S., Hirsch, S., Mazza, E., Székely, G., Falk, V., 2014. Image-based Mechanical Analysis of Stent Deformation. Concept and Exemplary Implementation for TAVI Stents. IEEE.

Goldenberg, G., Kusniec, J., Kadmon, E., Golovchiner, G., Zabarsky, R., Nevzorov, R., Vaknin, H., Assali, A., Kornowski, R., Haim, M.E.A., 2013. Pacemaker implantation after transcatheter aortic valve implantation. Am. J. Cardiol. 112 (10), 1632–1634.

Hall, G.J., Kasper, E.P., 2006. Comparison of element technologies for modeling stent expansion. J. Biomech. Eng. 128 (5), 751–756.

Jilaihawi, H., Chakravarty, T., Weiss, R.E., Fontana, G.P., Forrester, J., Makkar, R.R., 2012a. Meta-analysis of complications in aortic valve replacement: comparison of medtronic-corevalve, Edwards-SAPIEN and surgical aortic valve replacement in 8,536 patients. Catheter. Cardiovasc. Interv. 80 (1), 128–138.

Jilaihawi, H., Chin, D., Vasa-Nicotera, M., Jeilan, M., Spyt, T., Ng, G.A., Bence, J., Logtens, E., Kovac, J., 2009. Predictors for permanent pacemaker requirement after transcatheter aortic valve implantation with the corevalve bioprosthesis. Am. Heart J. 157 (5), 860–866.

Jilaihawi, H., Kashif, M., Fontana, G., Furugen, A., Shiota, T., Friede, G., Makhija, R., Doctor, N., Leon, M.B., Makkar, R.R., 2012b. Cross-sectional computed tomographic assessment improves accuracy of aortic annular sizing for transcatheter aortic valve replacement and reduces the incidence of paravalvular aortic regurgitation. J. Am. Coll. Cardiol. 59 (14), 1275–1286.

Khawaja, M.Z., Rajani, R., Cook, A., Khavandi, A., Moynagh, A., Chowdhary, S., Spence, M.S., Brown, S., Khan, S.Q., Walker, N.E.A., 2011. Permanent pacemaker insertion after corevalve transcatheter aortic valve implantation: incidence and contributing factors (the UK corevalve collaborative). Circulation 123 (9), 951–960.

Maurer, M., Röhrnbauer, B., Feola, A., Deprest, J., Mazza, E., 2014. Mechanical biocompatibility of prosthetic meshes: a comprehensive protocol for mechanical characterization. J. Mech. Behav. Biomed. Mater. 40, 42–58.

Mazza, E., Ehret, A.E., 2015. Mechanical biocompatibility of highly deformable biomedical materials. J. Mech. Behav. Biomed. Mater. 48, 100–124.

Moreno, R., Dobarro, D., Lopez de Sa, E., Prieto, M., Morales, C., Calvo Orbe, L., Moreno-Gomez, I., Filgueiras, D., Sanchez-Recalde, A., Galeote, G.E.A., 2009. Cause of complete atrioventricular block after percutaneous aortic valve implantation: insights from a necropsy study. Circulation 120 (5), e29–e30.

Morganti, S., Brambilla, N., Petronio, A., Reali, A., Bedogni, F., Auricchio, F., 2016. Prediction of patient-specific post-operative outcomes of TAVI procedure: the impact of the positioning strategy on valve performance. J. Biomech. 49 (12), 2513–2519.

Morganti, S., Conti, M., Aiello, M., Valentini, A., Mazzola, A., Reali, A., Auricchio, F., 2014. Simulation of transcatheter aortic valve implantation through patient-specific finite element analysis: two clinical cases. J. Biomech. 47 (11), 2547–2555.

QHull.org, 2016. Qhull Code for Convex Hull, Delaunay Triangulation, Voronoi Diagram, and Halfspace Intersection About a Point. URL ⟨http://www.qhull.org⟩.

Rubin, J.M., Avanzas, P., del Valle, R., Renilla, A., Rios, E., Calvo, D., Lozano, I., Anguera, I., Diaz-Molina, B., Cequier, A.E.A., 2011. Atrioventricular conduction disturbance characterization in transcatheter aortic valve implantation with the corevalve prosthesis. Circulation: Cardiovasc. Interv. 4 (3), 280–286.

Schultz, C., Rodriguez-Olivares, R., Bosmans, J., Lefevre, T., De Santis, G., Bruining, N., Collas, V., Dezutter, T., Bosmans, B., Rahhab, Z.E.A., 2016. Patient-specific image-based computer simulation for the prediction of valve morphology and calcium displacement after TAVI with the medtronic corevalve and the Edwards SAPIEN valve. EuroIntervention 11 (9), 1044–1052.

Sherif, M.A., Abdel-Wahab, M., Stcker, B., Geist, V., Richardt, D., Tölg, R., Richardt, G., 2010. Anatomic and procedural predictors of paravalvular aortic regurgitation after implantation of the medtronic corevalve bioprosthesis. J. Am. Coll. Cardiol. 56 (20), 1623–1629.

Takagi, K., Latib, A., Al-Lamee, R., Mussardo, M., Montorfano, M., Maisano, F., Godino, C., Chieffo, A., Alfieri, O., Colombo, A., 2011. Predictors of moderate-to-severe paravalvular aortic regurgitation immediately after corevalve implantation and the impact of postdilatation. Cathet. Cardiovasc. Interv. 78 (3), 432–443.